

Voltage-Controlled Topotactic Phase Transition in Thin-Film SrCoO_x Monitored by In Situ X-ray Diffraction

Qiyang Lu^{†,‡} and Bilge Yildiz^{*,†,‡,§}

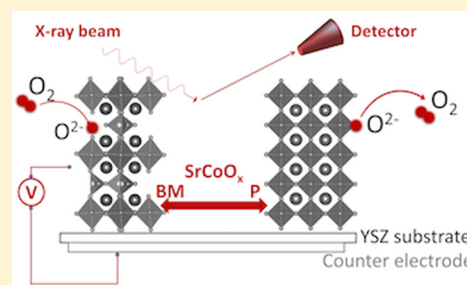
[†]Laboratory for Electrochemical Interfaces, Massachusetts Institute of Technology, Cambridge, Massachusetts 02139, United States

[‡]Department of Materials Science and Engineering, Massachusetts Institute of Technology, Cambridge, Massachusetts 02139, United States

[§]Department of Nuclear Science and Engineering, Massachusetts Institute of Technology, Cambridge, Massachusetts 02139, United States

S Supporting Information

ABSTRACT: Topotactic phase transition of functional oxides induced by changes in oxygen nonstoichiometry can largely alter multiple physical and chemical properties, including electrical conductivity, magnetic state, oxygen diffusivity, and electrocatalytic reactivity. For tuning these properties reversibly, feasible means to control oxygen nonstoichiometry-dependent phase transitions in functional oxides are needed. This paper describes the use of electrochemical potential to induce phase transition in strontium cobaltites, SrCoO_x (SCO) between the brownmillerite (BM) phase, $\text{SrCoO}_{2.5}$, and the perovskite (P) phase, $\text{SrCoO}_{3-\delta}$. To monitor the structural evolution of SCO, in situ X-ray diffraction (XRD) was performed on an electrochemical cell having (001) oriented thin-film SrCoO_x as the working electrode on a single crystal (001) yttria-stabilized zirconia electrolyte in air. In order to change the effective $p\text{O}_2$ in SCO and trigger the phase transition from BM to P, external electrical biases of up to 200 mV were applied across the SCO film. The phase transition from BM to P phase could be triggered at a bias as low as 30 mV, corresponding to an effective $p\text{O}_2$ of 1 atm at 500 °C. The phase transition was fully reversible and the epitaxial film quality was maintained after reversible phase transitions. These results demonstrate the use of electrical bias to obtain fast and easily accessible switching between different phases as well as distinct physical and chemical properties of functional oxides as exemplified here for SCO.



KEYWORDS: transitional metal oxides, perovskite, phase transition, in situ XRD

Transition metal oxides (TMOs) with the perovskite structure (ABO_3) are an attractive group of materials due to their highly tunable ionic and electronic transport properties.^{1–3} They function in energy storage and conversion devices, for instance, in solid oxide fuel cell (SOFC) electrodes,^{4,5} oxygen permeable membranes,⁶ and also in information storage and processing applications such as memristors⁷ and multiferroics.⁸ The nonstoichiometry in perovskites is typically associated with the presence of oxygen vacancies in the lattice that have a strong impact on their electrical transport and reactivity properties.⁹ The ability to precisely control oxygen nonstoichiometry is a prerequisite for being able to control perovskite oxide properties reversibly in energy and information applications.

A very large oxygen nonstoichiometry can be accommodated in some perovskite-related oxides, ABO_x with $x = 2.5$, by ordered oxygen vacancy channels. Examples include $\text{CaFeO}_{2.5}$,¹⁰ $\text{SrFeO}_{2.5}$,¹¹ and $\text{SrCoO}_{2.5}$.¹² Upon the formation of these ordered oxygen vacancy channels, the perovskite (P) phase is transformed to a brownmillerite (BM) phase, with alternating octahedral BO_6 and tetrahedral BO_4 layers ($\text{B} = \text{Fe}$ or Co). This topotactic phase transition enables one to store and release large amounts of oxygen by ordering and

disordering of oxygen vacancies. This ability is important for catalysis applications.^{13,14} Moreover, due to the distinct electrical¹¹ and magnetic¹⁵ properties of BM and P phases, controlling the oxygen nonstoichiometry and the associated phase can allow one to reversibly switch the physical properties of this oxide system. This ability is of particular interest for novel memory applications. One of the model systems for studying this phase change is strontium cobaltite, denoted as SCO, with the BM phase $\text{SrCoO}_{2.5}$ and the P phase $\text{SrCoO}_{3-\delta}$, where δ represents the oxygen substoichiometry. However, the oxidation from BM phase to P phase for bulk SCO is difficult, usually requiring a long time (tens of hours) of annealing in high oxygen pressure ($p\text{O}_2 > 50$ bar) at high temperatures (>300 °C),¹⁶ or the use of aggressive wet-chemical oxidants such as bromine.¹⁷ Recently, it was shown by Jeon et al.^{18,13} that SCO nanoscale thin films grown epitaxially on single crystal substrates can be reversibly oxidized and reduced in much milder conditions (~ 300 °C in 5 bar of $p\text{O}_2$) compared

Received: November 4, 2015

Revised: December 17, 2015

Published: December 21, 2015



to that required for bulk samples. Also, the kinetics for the phase transition is much faster due to extremely small diffusion lengths for oxygen to be incorporated into the thin films. This work noted the possibility to control the SCO catalytic, electrical, and magnetic properties within easily accessible temperature and oxygen pressure conditions. However, to switch the environment between the $p\text{O}_2$ of ~ 5 atm and $\sim 10^{-6}$ atm is still not feasible for practical device operation. Instead, if one can utilize an external stimulus to trigger the phase transition *without* changing the gas atmosphere, it would be more accessible and practical for reversibly controlling the electrical and magnetic properties of this material. Therefore, in this paper, we consider a solid state electrochemical method as a means to induce the phase transition based on oxygen nonstoichiometry without changing the atmosphere.

For an electrochemical system, one can change the chemical state of the electrode either by chemical stimuli or by electrical stimuli. Therefore, the nonstoichiometry of a solid oxide electrode can be changed both by $p\text{O}_2$ (chemical stimuli) and by applying an electrochemical potential on the electrode (electrical stimuli).⁵ The root of this method is in the Nernst equation, which states that an applied electrochemical potential, η , can change the oxygen partial pressure in the electrochemical system from the actual $p\text{O}_2$ in the environment to a different effective $p\text{O}_2$ level, $p\text{O}_2^{\text{eff}}$. The relation between η , $p\text{O}_2$, and $p\text{O}_2^{\text{eff}}$ as represented by the Nernst equation is

$$\eta = -\frac{RT}{4F} \ln \frac{p\text{O}_2}{p\text{O}_2^{\text{eff}}} \quad (1)$$

where R , T , and F are ideal gas constant, temperature, and Faraday constant, respectively. This $p\text{O}_2^{\text{eff}}$ induces a new equilibrium level of oxygen nonstoichiometry in the oxide. Electrical control of oxygen nonstoichiometry provides an elegant way of tuning the oxygen content in functional oxides without altering the environment atmosphere. For example, it was reported in literature for VO_2 that electrical gating via an ionic liquid can alter the oxygen vacancy content in VO_2 , which is responsible for the suppression of the metal–insulator transition.¹⁹ Recent work done by Kawada et al.²⁰ on $(\text{La,Sr})\text{CoO}_{3-\delta}$ (LSC) and Chen et al.²¹ on $(\text{Pr,Ce})\text{O}_{2-\delta}$ (PCO) also successfully validated this approach by tuning the nonstoichiometry δ electrically. They have calculated δ from the chemical capacitance deduced from electrochemical impedance spectroscopy (EIS) measurements. Instead, here, we use a structural feature of the lattice to assess the δ and the associated phase change. The oxygen nonstoichiometry affects the lattice parameter of reducible oxides due to the well-known phenomenon of chemical expansion.²² For most reducible oxides, the lattice expands when more oxygen vacancies are incorporated, as in the case of $\text{La}_{0.8}\text{Sr}_{0.2}\text{CoO}_3$ studied by Biegalski et al.²³ and $\text{La}_{0.6}\text{Sr}_{0.4}\text{Co}_{0.2}\text{Fe}_{0.8}\text{O}_3$ studied by Ingram et al.²⁴ In principle, in situ XRD also allows one to probe any phase transition induced by bias applied to an electrochemical system, as shown also by work done related to Li-ion battery electrodes.²⁵

The aim of this paper is to verify the concept of voltage-controlled oxygen nonstoichiometry and extend it to structural phase transition, by using SCO as a model system. This ability is important especially for memory applications where it is desirable to control the oxide properties reversibly by applied voltage. This is because, in the case of SCO, the change in oxygen nonstoichiometry not only leads to a lattice expansion/

contraction (as in the case of LSC or PCO mentioned above), but also importantly to a phase change and the emergence of distinct electrical and magnetic properties. We used in situ X-ray diffraction (XRD) to measure the lattice phase transitions in SCO, simultaneously with electrical biasing on solid oxide electrochemical cells. An external electrical bias was applied to the electrochemical cell consisting of a dense ~ 40 nm thick film of SCO as the working electrode, Y_2O_3 -stabilized ZrO_2 (YSZ) electrolyte with a Gd-doped CeO_2 (GDC) interlayer, and a porous Ag counter electrode. XRD measurements were performed in situ to probe the phase and lattice parameter of the SCO electrode while controlling the electrical bias, temperature, and oxygen pressure. The results clearly showed that one could tune the phase of SCO by applying an electrochemical potential reversibly.

The implication of this work is 2-fold. First, this work aims to demonstrate nonstoichiometry dependent phase transitions via voltage control in complex functional oxides using the model system SCO. Due to the highly distinct electrical conductivity of BM and P phases in this material, SCO is considered as a potential material for resistive switching (as memristor).²⁶ The mechanism for electric field induced change in the resistance state in SCO has not been clarified in literature,²⁶ although voltage-induced phase transition between BM and P was speculated as a likely mechanism. Therefore, the demonstration of reversible voltage control of the BM–P transitions can provide a more solid understanding of the mechanism behind resistive switching in SCO. The second implication is on the relevance of SCO and similar perovskite-related oxides for energy conversion and storage applications such as SOFC cathodes. It is important to assess the possible structural and chemical changes under nonopen circuit voltage conditions of such cathodes. Finite voltage conditions can induce a very large variation of effective $p\text{O}_2$ in the electrode material. If there is indeed a drastic change in the structure and chemical state in the oxide electrode, as can happen in SCO, then the ionic and electronic transport properties as well as the reactivity^{27,28} and stability²⁹ of these oxides are largely altered. Therefore, this work can be helpful for identifying the electrochemical potentials that lead to the transitions in phase and electrical properties at SCO electrodes.

Experimental Methods. Brownmillerite phase $\text{SrCoO}_{2.5}$ (BM-SCO) thin films were grown using pulsed laser deposition (PLD) on 8% yttria-stabilized zirconia (YSZ) substrates with (100) orientation (purchased from MTI Corp.). A KrF excimer laser with 248 nm wavelength was used. In order to prevent possible reaction between SCO and YSZ, a ~ 8 nm thick 10% gadolinium-doped ceria (GDC) buffer layer was deposited prior to the SCO deposition. Therefore, the sample structure can be denoted as SCO/GDC/YSZ. The substrate temperature was kept at 750 °C in an oxygen pressure of 20 mTorr. After deposition, the samples were cooled down to room temperature in the same oxygen pressure in order to prevent possible phase change. A Veeco Nanoscope IV atomic force microscope (AFM) operated at tapping mode was used to characterize the surface morphology of SCO thin films. In situ XRD at high temperature under different oxygen partial pressure was measured using a PANalytical X'Pert X-ray diffractometer with an Anton Parr HTK 1200N high-temperature oven chamber. Ultra high purity O_2 and N_2 were mixed using mass flow controllers with a flow rate of 200 sccm in order to achieve the desired oxygen partial pressure. The sample was equilibrated for 20 min before starting each measurement.

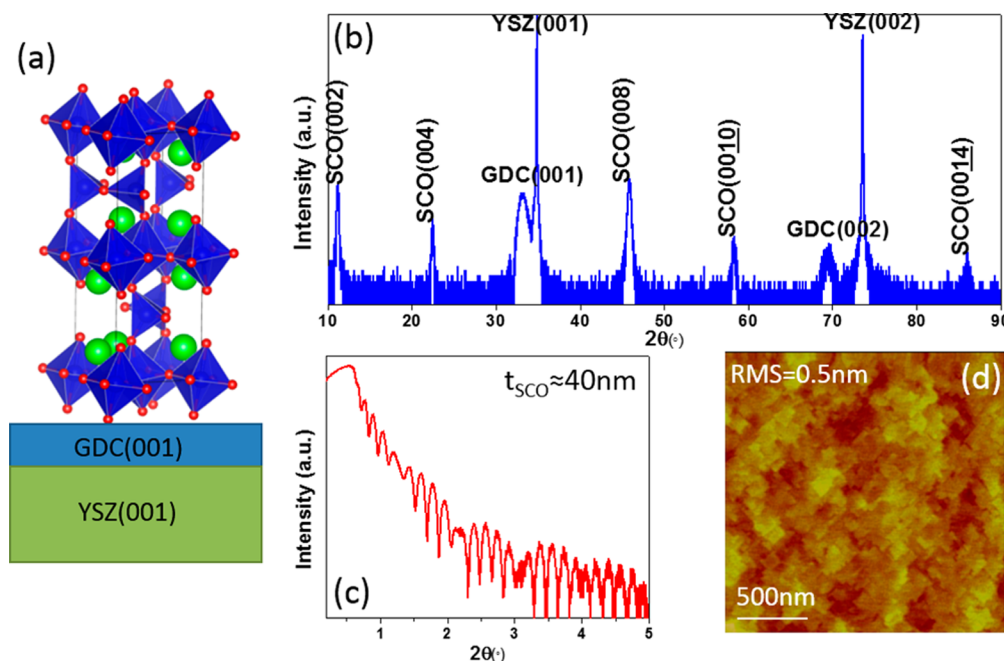


Figure 1. (a) Schematic (not to-scale) of the BM-SCO thin film on YSZ substrate with a GDC buffer layer. Red and green spheres represent the oxygen and strontium, respectively, and the cobalt is located at the centers of the octahedra and tetrahedra. (b) High-resolution X-ray diffraction data of 2θ - ω scan, (c) X-ray reflectivity data, and (d) the AFM image showing the surface morphology on the as-deposited SCO thin film.

The electrochemical cell has the structure of SCO/GDC/YSZ/Ag. Ag is the counter electrode (CE) that was made by applying Ag paste on the back of the YSZ substrate. In situ high-resolution high-temperature XRD at different electrical biases was measured on a Bruker D8 Discover X-ray diffractometer using 4-bounce Ge (022) monochromator and Cu $K\alpha 1$ radiation. An Anton Parr DHS 900 heating stage was used to heat the sample. Electrical feedthroughs made from Pt wires and ceramic sheaths were used to perform the electrical measurements. These wires were attached to sample top surface and bottom electrode using a small amount of silver paste. A Keithley 2400 SourceMeter was used to apply bias while recording current with time and was controlled using LabVIEW programs. We should note that total applied electrical bias was not all deposited as the electrochemical potential η on SCO WE, due to the voltage losses at the YSZ electrolyte, at the CE as well as at interfaces. To identify the η on the SCO WE, we calculate proportions of different voltage loss contributions using EIS measurements. This analysis of η is detailed in [Supporting Information](#), Figure S1.

Results and Discussion. Structural and surface morphology characterizations on SCO/GDC/YSZ samples are summarized in [Figure 1](#). High-resolution XRD 2θ - ω scan showed that SCO thin film grown on GDC/YSZ was (001)-oriented BM phase. This orientation indicates that the ordered structural oxygen vacancy channels in BM-SCO are parallel to the thin film surface, consistent with previous reports on thin SCO films.³⁰ The out-of-plane lattice parameter calculated from XRD data was $c = 15.8050 \text{ \AA}$, which is larger than the bulk lattice parameter of SCO ($c = 15.7450 \text{ \AA}$). This difference is likely due to the in-plane compressive strain introduced by the GDC buffer layer. GDC has a lattice parameter of $a = 5.3987 \text{ \AA}$, which is corresponding to $a/\sqrt{2} = 3.8174 \text{ \AA}$, whereas SCO has a larger pseudotetragonal lattice parameter of $a_t = 3.905 \text{ \AA}$. X-ray reflectivity (XRR) scan showed clear thickness fringes and a modulated pattern due to the two-layer thin film structure

including the SCO and GDC layers. This indicates good film quality and smooth interfaces. A film thickness of $\sim 40 \text{ nm}$ can be extracted from the XRR fringes. AFM image of a $2 \mu\text{m} \times 2 \mu\text{m}$ scan area showed a smooth surface and faceted surface terraces were visible. A root-mean-square (RMS) roughness of 0.5 nm was calculated based on the AFM image.

In order to examine any phase transition behavior induced by changing the oxygen partial pressure ($p\text{O}_2$) in the atmosphere at high temperature, in situ high-temperature XRD was performed. The sample was held at a constant temperature of $500 \text{ }^\circ\text{C}$, whereas the $p\text{O}_2$ in the furnace chamber was changed systematically from 10^{-5} to 1 atm . The results are shown in [Figure 2](#). Two diffraction peaks were monitored in order to detect possible phase change, and a clear difference in these two peaks was observed when the $p\text{O}_2$ was changed. BM phase (002) peak is the unique “fingerprint” for the presence of BM phase. It is a so-called half-order peak because the origin of this peak is the layered oxygen vacancy structure in BM phase. If the oxygen vacancies are disordered as in the case of P phase, then this peak should be suppressed. As shown in [Figure 2](#), the (002) peak disappeared when the oxygen partial pressure was increased from reducing condition at 10^{-5} atm to oxidation condition at 1 atm , which reveals that the thin film was transformed from BM phase to P phase. Also, the BM phase (008) diffraction peak was observed to shift to higher angles upon the phase transformed from BM to P. This is because P phase has a smaller lattice parameter compared to the BM phase. For example, for bulk samples at room temperature, BM phase has a lattice constant of $c/4 = 3.9363 \text{ \AA}$, whereas P phase has $a_p = 3.8289 \text{ \AA}$. In summary, in situ XRD data at $500 \text{ }^\circ\text{C}$ showed that BM-SCO thin film can be transformed to P-SCO by simply increasing $p\text{O}_2$ to 1 atm . Compared to the temperature and $p\text{O}_2$ needed for transforming bulk SCO reported in literature,¹⁶ this condition is more feasible.

[Figure 3](#) summarizes the results of XRD experiments with electrical biasing at $500 \text{ }^\circ\text{C}$ and $p\text{O}_2 = 0.21 \text{ atm}$ on the

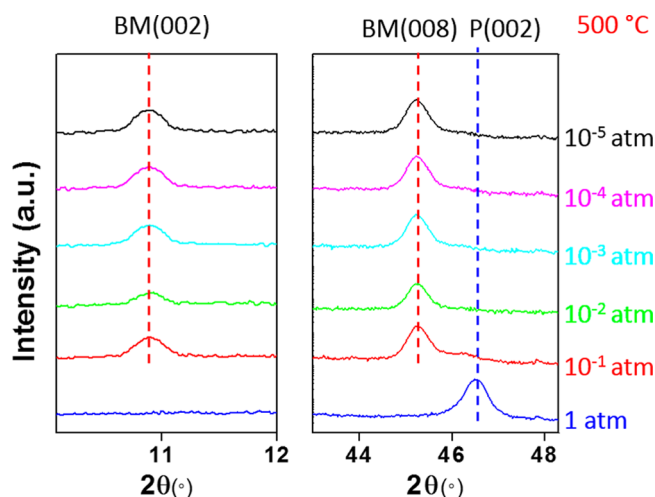


Figure 2. In situ XRD results on SCO thin film sample at 500 °C as a function of oxygen gas pressure, pO_2 . BM phase (002) peak and (008) peak are shown marked by dashed lines. Upon phase transition from BM-SCO to P-SCO, the BM (008) peak is transformed to the P (002) peak and the BM (002) peak disappears.

electrochemical cell. Similar to that in Figure 2, two diffraction peaks, that is, the BM-SCO (002) and (008) peaks, were highlighted to follow the phase transition in the SCO thin film. Both peaks showed clear changes as the applied electrical bias was increased from 0 mV up to 200 mV. Impedance spectroscopy showed that about 75% of the applied bias was on SCO WE (Supporting Information, Figure S1). Therefore, the maximum electrochemical potential applied at the SCO electrode in these experiments was ~ 150 mV. For identifying

the phase transition conditions, in the rest of the paper, we will refer to the electrochemical potential applied on SCO WE instead of the total electrical bias applied on the cell. The half-order BM-SCO (002) peak (Figure 3a) was present when no bias was applied, consistent with the starting phase being BM, and remained the same up to 22.5 mV of electrochemical potential on SCO. When the SCO potential was increased above 22.5 mV, the intensity of the peak decreased and finally was fully suppressed. The suppression of this peak proves that oxygen intercalated into the SCO thin film and disordered the vacancy structure while transforming the thin film to P phase. This bias-induced phase transition is also supported by the change in the BM (008) peak, shown in Figure 3b. The BM (008) peak is at $2\theta = 45.318^\circ$ without any bias applied. When 22.5 mV of electrochemical potential was applied, an extra peak at higher 2θ position of 46.290° appeared, consistent with the position of the P (002) peak. This extra peak suggests that the film is partially transformed to the P phase. When higher bias was applied, the BM (008) peak was suppressed and only the higher angle P (002) peak is present. Again, this peak shift explicitly shows that the applied electrochemical potential on SCO induces the phase transition in SCO from BM to P.

The pO_2^{eff} in the SCO electrode (also shown in Figure 3) can be calculated using the Nernst equation as described above. In this experiment, pO_2 is the oxygen partial pressure in the atmosphere, which is 0.21 atm, and temperature is 773 K, and η is the electrochemical potential drop between the SCO electrode surface and SCO/YSZ interface. On the basis of η between 22.5 mV to 30 mV for the transition point, pO_2^{eff} at the onset of BM \rightarrow P phase transition is found as ~ 1 atm (between 0.81 atm effectively at 22.5 mV and 1.27 atm effectively at 30

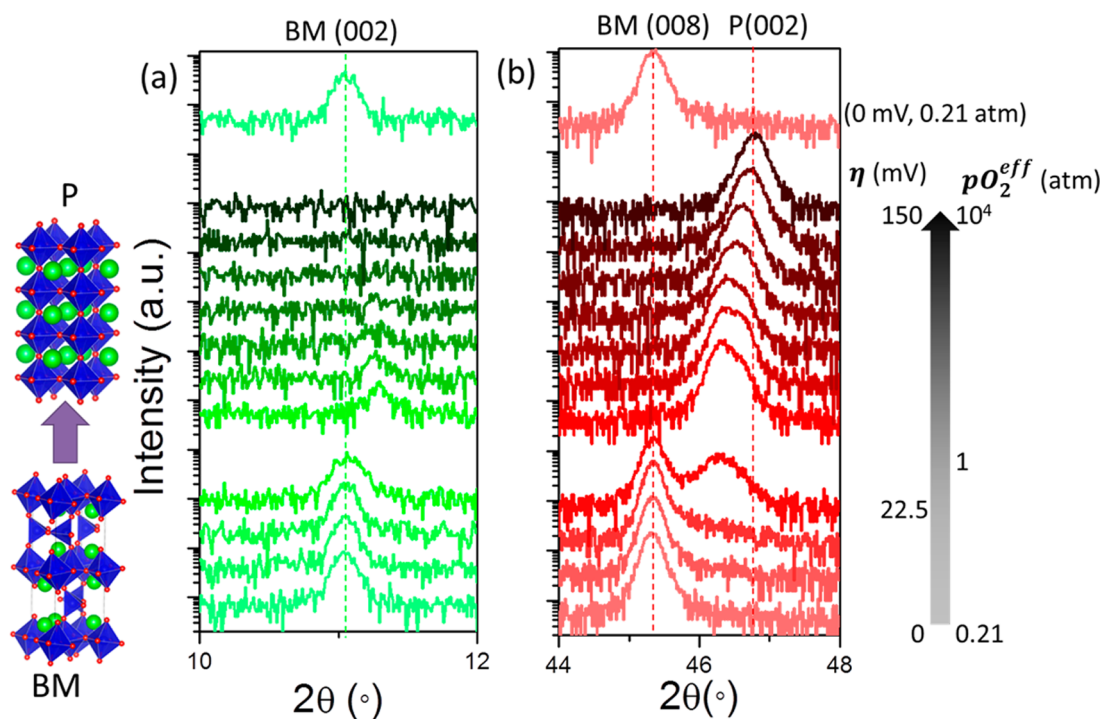


Figure 3. In situ XRD results on SCO thin film when different electrochemical potentials were applied at 773 K and 0.21 atm of pO_2 . The changes in two diffraction peaks, (a) the BM-SCO (002) peak (half-order peak) and (b) the BM-SCO (008) or P-SCO (002) peak are shown as a function of applied electrochemical potential, η , at the SCO electrode. The effective oxygen pressure, pO_2^{eff} , was calculated based on the electrochemical potential at the SCO electrode according to the Nernst equation described in eq 1. On the left images of SCO, the red and green spheres represent the oxygen and strontium, respectively, and the cobalt is located at the centers of the octahedra and tetrahedra.

mV). This value is consistent with the phase transition found at ~ 1 atm by varying only the $p\text{O}_2$ at 773 K as shown in Figure 2. This finding shows that $p\text{O}_2$ that is effectively changed by electrical stimuli has the same result on the BM \rightarrow P phase transition induced by oxygen nonstoichiometry as does the actual gas $p\text{O}_2$.

One crucial point for this study is that the surface exchange reaction has to be rate limiting for the Nernst eq (eq 1) to be valid. In this experiment, we believe that the kinetics of oxygen incorporation at the SCO electrode surface, rather than the oxygen diffusion in the SCO bulk, is the rate-limiting step. This is based on the following two facts. First, the electrochemical impedance spectroscopy (EIS) data, which were collected during in situ XRD measurements, did not show the characteristics for a diffusion-limited rate-limiting step (Figure S1 in Supporting Information). If oxygen diffusion is the limiting step, then the EIS data should show a Warburg element with 45° straight line at the low-frequency regime. However, we did not observe that, and on the contrary, a slightly compressed semicircle was observed at low frequency, which is typical for cases limited by surface oxygen incorporation. Second, as noted above in Figure 3, we compared the structural evolution of the SCO electrode by only changing the actual gas $p\text{O}_2$ in the environment and by applying electrochemical potential. We found that these two results were equivalent, that is, the BM \rightarrow P phase transition can be triggered either by an actual $p\text{O}_2$ of about 1 atm, and by the electrochemical potential applied on SCO to give a $p\text{O}_2^{\text{eff}}$ of about 1 atm. We note that this consistency can only be achieved when the oxygen diffusion in SCO is not rate-limiting. If the oxygen diffusion is the rate-limiting step, then there will be a gradient of $p\text{O}_2^{\text{eff}}$ inside the SCO electrode bulk. This would require then a much higher electrochemical potential applied to obtain the $p\text{O}_2^{\text{eff}}$ above 1 atm in the whole thin film to be transformed to P-SCO. However, this is not what we found. Therefore, we can assert that in our case, the oxygen surface incorporation is the rate-limiting step during in situ XRD measurements.

The BM (008) and the P (002) peaks were used for calculating the out-of-plane lattice parameters of SCO thin film as a function of electrochemical potential applied on SCO as shown in Figure 4. A sharp drop at around 22.5 mV was found. With increasing potential, the lattice parameter of SCO becomes smaller, especially for the P-SCO phase due to chemical contraction.^{22,31} An increasing positive electro-

chemical potential increases the $p\text{O}_2^{\text{eff}}$ in SCO, decreases the oxygen vacancy concentration, and thus, decreases the lattice parameter. Lattice contraction with increasing effective $p\text{O}_2$ found here is consistent with the behavior of other perovskite oxides.³¹

In order to assess whether the SCO film retains its physical integrity and epitaxy during phase transformation, the change of in-plane lattice parameter during the phase transition was probed by in situ reciprocal space mapping (RSM). Figure 5 shows the results of RSM on SCO thin film at 300 $^\circ\text{C}$. The BM-SCO (10 $\bar{1}2$) spot was present in the reciprocal space at 300 $^\circ\text{C}$ without any applied bias. By calculating the lattice parameter from q_x in RSM, we found that the in-plane compressive strain is partially relaxed, which is presumably due to the relatively large thickness of the thin-film SCO (~ 40 nm) and the relatively large lattice mismatch between BM-SCO ($a = 3.905$ Å) and GDC ($a/\sqrt{2} = 3.817$ Å). Upon anodic bias application, BM-SCO (10 $\bar{1}2$) spot disappeared and the P-SCO (103) spot appeared at a higher q_z position. The key point from Figure 5 is that while the q_z clearly changed, the q_x position did not change during the transition from BM to P phase. The increasing of q_z indicates a decrease in the out-of-plane lattice parameter from BM to P phase, consistent with the out-of-plane lattice parameter deduced from the 2θ – ω scans and plotted in Figure 4. The unchanged q_x reveals that the in-plane lattice parameter of SCO thin films were essentially clamped by the substrates and was not free to move during the phase transition. The clamping of the in-plane lattice parameter can introduce large stresses to the oxide thin film during the phase transition. Here, however, the lattice parameter of the P-SCO is smaller than that of the BM-SCO, and therefore, it is closer to that of the GDC interlayer. It is intriguing and worthwhile to further investigate in the future whether this reduced mismatch (stress) at the film/substrate interface has any facilitating effect on the phase transition of SCO in thin film structures.

The phase transformation from BM-SCO to P-SCO is also seen in the electrical signature of the thin film sample. The chronoamperometry (i.e., current–time, I – t) curves were measured during the in situ XRD experiment, as summarized in Figure 6. The process taking place in the electrochemical cell upon application of an external potential is similar to potentiostatic coulometric titration. Therefore, one would expect an exponential-like relaxation curve for the measured I – t curve³² if the electrode does not change its phase. However, the measured I – t curves under high electrochemical potential behaved anomalously and did not show a simple exponential relaxation. Figure 6a,b highlights the evolution of the I – t curves with increasing electrochemical potential at the SCO electrode. The striking feature shown here is that the I – t curve shapes started to deviate from single-exponential curves, developing to shapes with an inflection point. This deviation can be observed in the early stage under an electrochemical potential of ~ 30 mV, which is near the transitional point from BM to P phase as shown in Figure 3. Under higher electrochemical biases, the shapes of the I – t curves were changed more appreciably. Therefore, it is reasonable to attribute this deviation in the kinetics of the electrical relaxation to the phase transition from BM to P phase in the SCO film. The change of kinetics possibly arises from a different surface oxygen exchange reactivity of the BM-SCO versus the P-SCO phases or from a difference in the chemical capacitance of these two phases due to distinct oxygen nonstoichiometry. Similar changes in the chronoamperometry behavior was observed during the charging/discharging process

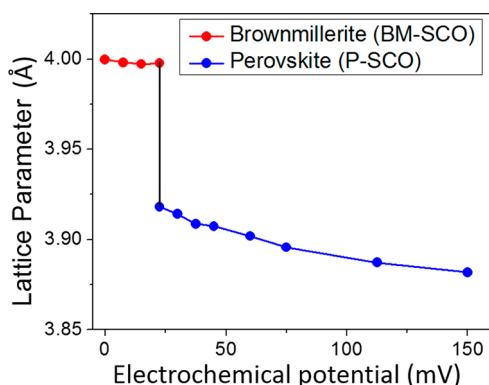


Figure 4. Out-of-plane lattice parameters of BM-SCO and P-SCO extracted from in situ XRD data shown in Figure 3, as a function of electrochemical potential at the SCO electrode, collected at 500 $^\circ\text{C}$ in air.

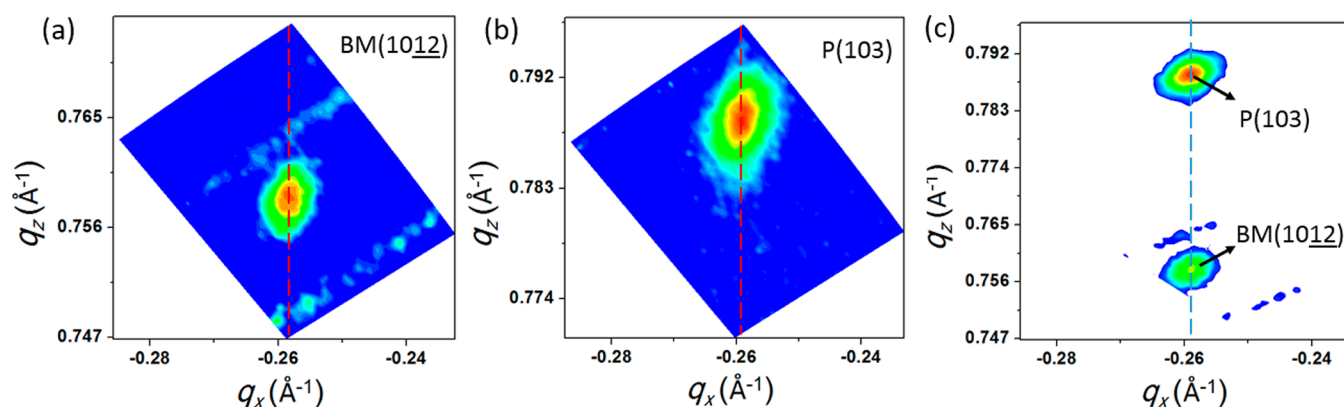


Figure 5. In situ reciprocal space maps (RSM) collected for (a) BM-SCO, without bias applied and (b) P-SCO upon phase transition from BM to P with 4 V applied bias. q_x and q_z are the in-plane and out-of-plane reciprocal lattice spacings, respectively. The BM(1012) peak was measured at 300 °C with no bias applied. The P(103) peak was measured when a bias of 4 V was applied to the electrochemical cell. In (a) and (b), the vertical dashed lines indicate the reciprocal in-plane lattice parameters. (c) RSM combining both the P(103) and the BM(1012) diffraction spots, which were observed one at a time, as indicated in (a) and (b). The dashed line indicates that the in-plane lattice parameter is essentially the same for BM and P phases before and after the phase transition.

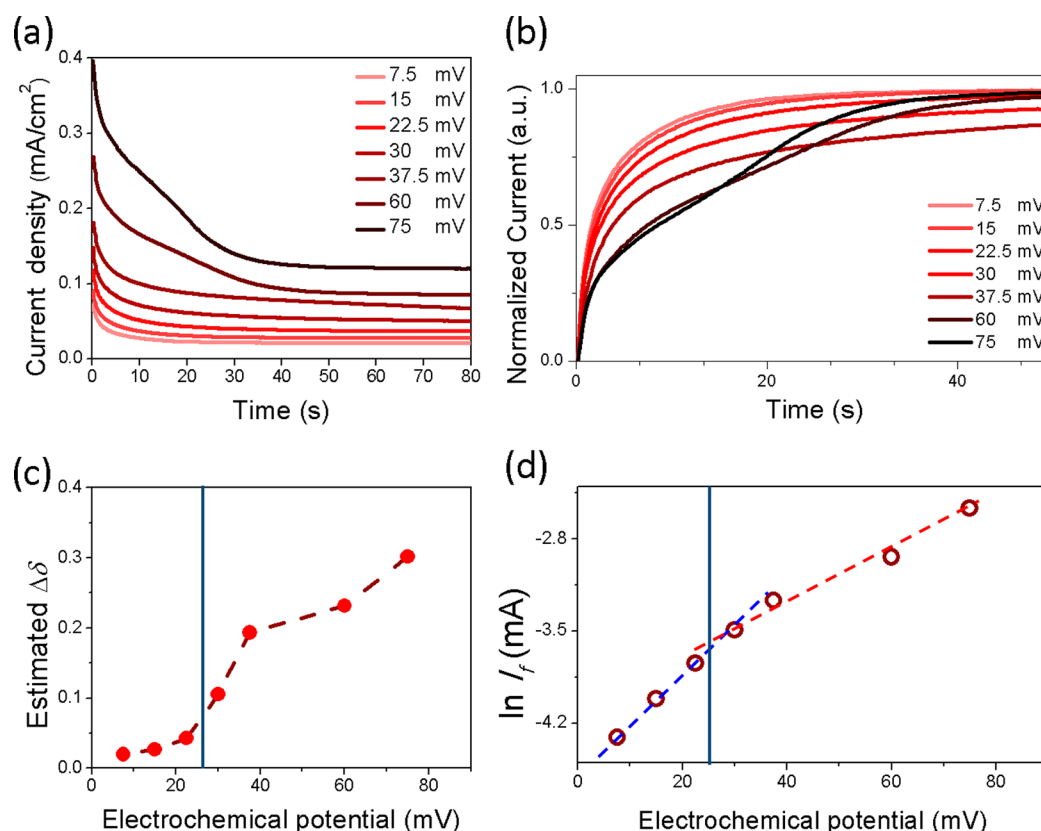


Figure 6. (a) Current–time (I – t) curves under electrochemical potential from 7.5 mV to 75 mV applied on the SCO electrode, measured at 500 °C in air. (b) Normalized current–time (I – t) curves. The normalization is calculated using initial current I_i and final equilibrium current I_f (saturated current), the normalized current $I_n(t) = (I(t) - I_i)/(I_f - I_i)$. The time axis is zoomed in to the earlier stages of the relaxation in order to highlight the shape change of the I – t curves with increasing electrochemical potential. (c) Change of oxygen nonstoichiometry, that is, $\Delta\delta$, as a function of applied electrochemical potential. $\Delta\delta$ is defined to represent the change of the oxygen concentration as a function of bias in the SCO lattice starting from the BM phase, that is, change from $\text{SrCoO}_{2.5}$ to $\text{SrCoO}_{2.5+\Delta\delta}$. The vertical line marks the electrochemical potential at the on-set of the BM \rightarrow P phase transition in SCO (~ 26 mV, which corresponds to a $p\text{O}_2^{\text{eff}}$ of 1 atm, as shown in Figure 3). The $\Delta\delta$ was calculated from the I – t curves, see Figure S3 (Supporting Information) for details. The connecting lines are a guide for the eye. (d) Semilog plot of saturated current, I_f , as a function of the electrochemical potential on SCO. The vertical line marks the BM \rightarrow P transition potential, same as in (c). Notice the slope change around the phase transition potential.

in Li-ion battery cathode materials such as Li_xFePO_4 .³³ In that case, too, the deviation from a simple exponential relaxation in the I – t curves was attributed to the phase transformation. In

our experiment, the I – t curves are a superposition of multiple processes, including the oxygen reduction at the Ag CE electrode, charge transfer at Ag/YSZ and YSZ/SCO interfaces,

as well as the oxygen incorporation in the SCO electrode. Therefore, it is difficult to extract quantitative information from these curves currently for modeling and reproducing the phase transition kinetics. Future work will focus on that activity. Nevertheless, two additional important pieces of information can be extracted from further analysis of the I - t curves, shown in Figure 6c,d. First, the oxygen nonstoichiometry change, $\Delta\delta$, of the SCO electrode was calculated from the I - t curves (see Supporting Information, Part III for details. Here, the $\Delta\delta$ is defined to represent the change of the oxygen concentration as a function of bias in the SCO lattice starting from the BM phase, that is, change from $\text{SrCoO}_{2.5}$ to $\text{SrCoO}_{2.5+\Delta\delta}$). $\Delta\delta$ is plotted in Figure 6c as a function of electrochemical potential on SCO. It is interesting to note that, although the $\Delta\delta$ prior to the BM \rightarrow P phase transition was relatively small, it increases significantly after the BM \rightarrow P phase transition. This suggests that the oxygen stoichiometry of BM-SCO remains close to 2.5, whereas the P-SCO can accommodate a larger oxygen nonstoichiometry. This is consistent with the more appreciable and continuous chemical expansion behavior of the P phase compared to that in the BM phase, shown in Figures 3 and 4. Second, the so-called Tafel plot, that is, the relationship between final equilibrium current I_f and the applied electrochemical potential is shown in Figure 6d. The slopes and the extrapolated intercepts obtained before and after the BM \rightarrow P transition potential are evidently different. This difference can be tentatively attributed to the difference in the oxygen surface incorporation rate of the BM vs the P phase of SCO.

Conclusion. In conclusion, the electrochemically driven topotactic phase transition of SCO was studied utilizing in situ XRD and RSM. We found that the BM \rightarrow P phase transition of SCO can be feasibly induced by applying anodic electrochemical bias to control the oxygen nonstoichiometry of the SCO electrode. An electrochemical potential as low as 22.5 mV applied at the SCO electrode could readily induce the phase transition of SCO from the BM to the P phase at 500 °C in air. The removal of the bias under the same conditions reverses the phase back to the BM structure. In situ RSM measurements demonstrated that the phase transition was fully reversible while retaining the physical integrity of the epitaxial SCO film. Moreover, I - t curves changed their shape at biases that induce the phase transition, and this change suggests that the oxygen incorporation kinetics is also altered because of the different surface exchange properties of the BM and P phases of SCO. Analysis of the I - t data also revealed that the oxygen stoichiometry of BM-SCO remains close to 2.5, whereas the P-SCO can accommodate a larger oxygen nonstoichiometry change after the phase transition.

In situ XRD revealed an abrupt decrease in the out-of-plane lattice parameter upon BM \rightarrow P phase transition consistent with the relative lattice sizes of these phases, and also a substantial chemical contraction for the P-SCO upon electrochemical oxidation. This chemomechanical coupling induced by bias has two implications. First, if SCO is used as solid oxide electrode, which is usually operated under conditions far from equilibrium, that is, the effective $p\text{O}_2$ can be substantially different from environmental $p\text{O}_2$, then one needs to pay attention to possible chemical expansion/contraction introduced by electrical loading and subsequent stress in electrodes. Second, because there is strong coupling between the chemical properties and the structure of SCO, it might be possible to use strain engineering to tune the phase and properties of SCO.

The feasible transition from BM to P phase of SCO achieved by electrochemical potential reported here opens up new paths of using voltage to control the phase, and more importantly, the physical properties of functional oxides. This ability is of specific interest to redox-based resistive switches as novel memory devices and to oxide (electro-) catalysts. We believe that the findings in this paper deepen the understanding of the resistive switching mechanism in SCO and, more generally, of the effects of electrical bias in tuning the functionality of oxides.

■ ASSOCIATED CONTENT

§ Supporting Information

The Supporting Information is available free of charge on the ACS Publications website at DOI: 10.1021/acs.nanolett.5b04492.

Details about electrochemical impedance spectroscopy data; additional discussion on diffraction peak width change during phase transition; details on the calculation of change in oxygen nonstoichiometry. (PDF)

■ AUTHOR INFORMATION

Corresponding Author

*E-mail: byildiz@mit.edu.

Notes

The authors declare no competing financial interest.

■ ACKNOWLEDGMENTS

The authors acknowledge the funding support from the MIT MRSEC through the MRSEC Program of the National Science Foundation under Award No. DMR-1419807. The authors would also like to acknowledge discussions with Prof. Harry Tuller and Dr. Di Chen of MIT on their work of controlling oxygen nonstoichiometry electrochemically in doped ceria, which inspired this work on phase transitions in SCO.

■ REFERENCES

- (1) Maier, J. *Nat. Mater.* **2005**, *4*, 805–815.
- (2) Nørskov, J. K.; Bligaard, T.; Rossmeisl, J.; Christensen, C. H. *Nat. Chem.* **2009**, *1*, 37–46.
- (3) Suntivich, J.; Gasteiger, H. a; Yabuuchi, N.; Nakanishi, H.; Goodenough, J. B.; Shao-Horn, Y. *Nat. Chem.* **2011**, *3*, 546–550.
- (4) Tuller, H. L.; Bishop, S. R. *Annu. Rev. Mater. Res.* **2011**, *41*, 369–398.
- (5) Chueh, W. C.; Haile, S. M. *Annu. Rev. Chem. Biomol. Eng.* **2012**, *3*, 313–341.
- (6) Hendriksen, P. V.; Larsen, P. H.; Mogensen, M.; Poulsen, F. W.; Wiik, K. *Catal. Today* **2000**, *56*, 283–295.
- (7) Waser, R.; Dittmann, R.; Staikov, G.; Szot, K. *Adv. Mater.* **2009**, *21*, 2632–2663.
- (8) Schlom, D. G.; Chen, L.-Q.; Fennie, C. J.; Gopalan, V.; Muller, D. a; Pan, X.; Ramesh, R.; Uecker, R. *MRS Bull.* **2014**, *39*, 118–130.
- (9) Boehm, E.; Bassat, J. M.; Dordor, P.; Mauvy, F.; Grenier, J. C.; Stevens, P. *Solid State Ionics* **2005**, *176*, 2717–2725.
- (10) Inoue, S.; Kawai, M.; Ichikawa, N.; Kageyama, H.; Paulus, W.; Shimakawa, Y. *Nat. Chem.* **2010**, *2*, 213–217.
- (11) Kozhevnikov, V. L.; Leonidov, I. a.; Patrakeeve, M. V.; Mitberg, E. B.; Poeppelmeier, K. R. *J. Solid State Chem.* **2001**, *158*, 320–326.
- (12) Le Toquin, R.; Paulus, W.; Cousson, A.; Prestipino, C.; Lamberti, C. *J. Am. Chem. Soc.* **2006**, *128*, 13161–13174.
- (13) Jeen, H.; Choi, W. S.; Biegalski, M. D.; Folkman, C. M.; Tung, I.-C.; Fong, D. D.; Freeland, J. W.; Shin, D.; Ohta, H.; Chisholm, M. F.; Lee, H. N. *Nat. Mater.* **2013**, *12*, 1057–1063.
- (14) Ezbiri, M.; Allen, K. M.; Gálvez, M. E.; Michalsky, R.; Steinfeld, A. *ChemSusChem* **2015**, *8*, 1966–1971.

- (15) Xie, C. K.; Nie, Y. F.; Wells, B. O.; Budnick, J. I.; Hines, W. a.; Dabrowski, B. *Appl. Phys. Lett.* **2011**, *99*, 052503.
- (16) Taguchi, H.; Shimada, M.; Koizumi, M. *J. Solid State Chem.* **1979**, *29*, 221–225.
- (17) Karvonen, L.; Valkeapää, M.; Liu, R.-S.; Chen, J.-M.; Yamauchi, H.; Karppinen, M. *Chem. Mater.* **2010**, *22*, 70–76.
- (18) Jeon, H.; Choi, W. S.; Freeland, J. W.; Ohta, H.; Jung, C. U.; Lee, H. N. *Adv. Mater.* **2013**, *25*, 3651–3656.
- (19) Jeong, J.; Aetukuri, N.; Graf, T.; Schladt, T. D.; Samant, M. G.; Parkin, S. S. P. *Science* **2013**, *339*, 1402–1405.
- (20) Kawada, T.; Suzuki, J.; Sase, M.; Kaimai, a.; Yashiro, K.; Nigara, Y.; Mizusaki, J.; Kawamura, K.; Yugami, H. *J. Electrochem. Soc.* **2002**, *149*, E252.
- (21) Chen, D.; Tuller, H. L. *Adv. Funct. Mater.* **2014**, *24*, 7638–7644.
- (22) Bishop, S. R.; Marrocchelli, D.; Chatzichristodoulou, C.; Perry, N. H.; Mogensen, M. B.; Tuller, H. L.; Wachsman, E. D. *Annu. Rev. Mater. Res.* **2014**, *44*, 205–239.
- (23) Biegalski, M. D.; Crumlin, E.; Belianinov, a.; Mutoro, E.; Shao-Horn, Y.; Kalinin, S. V. *Appl. Phys. Lett.* **2014**, *104*, 161910.
- (24) Ingram, B. J.; Eastman, J. a.; Chang, K.-C.; Kim, S. K.; Fister, T. T.; Perret, E.; You, H.; Baldo, P. M.; Fuoss, P. H. *Appl. Phys. Lett.* **2012**, *101*, 051603.
- (25) Andersson, A. S.; Kalska, B.; Haggstrom, L.; Thomas, J. O. *Solid State Ionics* **2000**, *130*, 41–52.
- (26) Tambunan, O. T.; Parwanta, K. J.; Acharya, S. K.; Lee, B. W.; Jung, C. U.; Kim, Y. S.; Park, B. H.; Jeong, H.; Park, J.-Y.; Cho, M. R.; Park, Y. D.; Choi, W. S.; Kim, D.-W.; Jin, H.; Lee, S.; Song, S. J.; Kang, S.-J.; Kim, M.; Hwang, C. S. *Appl. Phys. Lett.* **2014**, *105*, 063507.
- (27) Fleig, J. *Annu. Rev. Mater. Res.* **2003**, *33*, 361–382.
- (28) Sengodan, S.; Choi, S.; Jun, A.; Shin, T. H.; Ju, Y.-W.; Jeong, H. Y.; Shin, J.; Irvine, J. T. S.; Kim, G. *Nat. Mater.* **2014**, *14*, 205–209.
- (29) Backhaus-Ricoult, M.; Adib, K.; St. Clair, T.; Luerssen, B.; Gregoratti, L.; Barinov, a. *Solid State Ionics* **2008**, *179*, 891–895.
- (30) Jeon, H.; Bi, Z. H.; Choi, W. S.; Chisholm, M. F.; Bridges, C. A.; Paranthaman, M. P.; Lee, H. N. *Adv. Mater.* **2013**, *25*, 6459–6463.
- (31) Perry, N. H.; Kim, J. J.; Bishop, S. R.; Tuller, H. L. *J. Mater. Chem. A* **2015**, *3*, 3602–3611.
- (32) Maier, J. *Physical Chemistry of Ionic Materials: Ions and Electrons in Solids*; John Wiley & Sons: Chichester, England/Hoboken, NJ, 2004.
- (33) Oyama, G.; Yamada, Y.; Natsui, R.; Nishimura, S.; Yamada, a. *J. Phys. Chem. C* **2012**, *116*, 7306–7311.